A Mathematical Model for the Analysis of Eye Fundus Images in Healthy and Diabetic Patients

Arianna Travaglini[1,2] and Gianluca Vinti[1(✉)]

[1] Department of Mathematics and Computer Science, University of Perugia, 1, Via Vanvitelli, 06123 Perugia, Italy
arianna.travaglini@unifi.it, gianluca.vinti@unipg.it
[2] Department of Mathematics and Computer Science "U.Dini" - DIMAI, University of Florence, 67/a, Viale Giovanni Battista Morgagni, 50134 Firenze, Italy

Abstract. In this paper, we provide a study on eye fundus images of healthy and diabetic patients. Taking benefits from its reconstruction and enhancing properties, the sampling Kantorovich algorithm is used to process the considered images, after registration and averaging processes. Moreover, a hybrid segmentation procedure applied on superficial capillary plexus images (SCP) and one using the local Phansalkar method on choriocapillary images (CC) are exploited in order to asses a cluster counting process which is based on finding connected regions according to the 8–*adjacency* criterion. The results achieved on the healthy and diabetic patients show that the novel strategy allows to obtain accurate data from both a mathematical and a clinical point of view.

Keywords: SK algorithm · approximation results · digital image processing · registration · segmentation · cluster counting · diabetic patients

1 Introduction

The optical coherence tomography angiography (OCTA) is a relatively new technique used in ocular medical imaging in order to obtain visual representation of the ocular fundus [1]. Even if fluorangiography is considered the best imaging technique to represent the deep eye tissue, it requires the injection of a contrast agent. Instead, OCTA is a non invasive technique, since provides the visualization of the retinal perfusion without injection of any contrast agent. However,

A. Travaglini and G. Vinti have been partially supported within the 2022 GNAMPA-INdAM Project "Enhancement e segmentazione di immagini mediante operatori di tipo campionamento e metodi variazionali per lo studio di applicazioni biomediche" and G. Vinti within the projects Ricerca di Base 2019 dell'Università degli Studi di Perugia— "Integrazione, Approssimazione, Analisi Nonlineare e loro Applicazioni" and "Innovation, digitalisation and sustainability for the diffused economy in Central Italy - VITALITY (proposal identification code n. ECS_00000041)".

© The Author(s), under exclusive license to Springer Nature Switzerland AG 2023
O. Gervasi et al. (Eds.): ICCSA 2023 Workshops, LNCS 14108, pp. 558–576, 2023.
https://doi.org/10.1007/978-3-031-37117-2_38

it has some limitations such as artifacts, which may be due to the OCT image acquisition itself or eye motion. For this reasons, many studies on image quality enhancement and noise reduction have been carried out (see, e.g., [2,3]) and more are still going on. In [4] a study on SCP (superficial capillary plexus) and CC (choriocapillary plexus) of healthy patients has been carried out using mainly the above techniques.

In this paper we want to extend the research on diabetic patients, who are potentially characterized by diseased eyes. Indeed, diabetes can cause diabetic macular edema, which is a swelling of the macula [5]. This condition has the potential to gradually obliterate the sharp vision in this area of the eye, resulting in partial vision loss or blindness.

The main purpose of this study is to improve the quality of OCTA eye images (both SCP and CC) coming from 20 healthy and 16 diabetic subjects, by applying a series of digital image processing techniques. For each healthy patient eye, six SCP images and six CC images were acquired by the OCTA scan; while for diabetic subjects we have at disposal five SCP and five CC images. At first, image registration techniques are performed in order to overlap each SCP image with the target one, chosen as the less noisy. The same coordinates are used to register are the CC images, since it is possible to assume that the choriocapillary tissue is rigidly connected to the superficial capillary plexus. Then, the resulting images are averaged and, resized and filtered by the SK algorithm, which consists in the implementation of the reconstruction (convergence) result of a given signal/image by means of the sampling Kantorovich operators (see, e.g., [6,7]).

For these operators, approximation results in the general setting of Orlicz spaces and, in particular, in L^p-spaces, as well as in the space of continuous and uniformly continuous functions, were provided in previous studies (see, e.g., [6–13]).

The SK algorithm, which behaves simultaneously as a low-pass filter and as a rescaling method for the increasing of the information content of images, plays a crucial role in the entire process exploited in this work. Indeed, it has been proved to be a powerful mathematical tool for the reconstruction and improvement of images. In this sense, several interesting outcomes have been attained as a result of this implementation, both in the engineering and biomedical fields [4,14–20]. Additionally, we note that the SK algorithm's efficiency in image rescaling has been assessed in relation with some interpolation and quasi-interpolation techniques, in terms of PSNR and CPU time [21].

In order to deduce quantitative assessments which could allow a comparison between healthy and diabetic patients, a *cluster counting* process has been adopted. This method is based on the fact that the eye vessels' network tends to be fully connected, i.e. it is ideally possible to go through all the capillaries with a single path, (arguments in favor of this assumption can be found in [22]). In order to do this, a segmentation process, which exploits a hybrid thresholding technique presented in [4], has been used on SCP images, starting from the well–known Otsu [23] and Phansalkar [24] local methods; the latter, which is particularly suitable when dealing with images characterized by a nonuniform

staining, has been instead used on CC images (see, e.g., [25,26]). As mentioned above, since the vascularization of the retina is assumed to be fully connected, the selected criterion for the cluster counting analysis is that of the 8–adjacency.

Finally, the cluster counting assessment results important also for estabilishing a comparison between the only averaged image and that reconstructed with the SK algorithm after the averaging process, both for healthy and diabetic patients.

The paper is organized as follows: in Sect. 2 we report the fundamental approximation results for the family of sampling Kantorovich operators as well as some examples of kernels, whose choice plays a fundamental role in the application of the SK algorithm. In Sect. 3, the main methods for the processing of the considered images are described, i.e. the SK algorithm and the others digital image processing (DIP) techniques that are helpful for the whole procedure. The segmentation methods for the cluster counting analysis are described in Sect. 4. The experimental data are provided in Sect. 5, while in Sect. 6 we present the numerical achievements of the current study. Finally, Sect. 7 summarizes some remarks for the conclusions of the paper.

2 Approximation Properties of Sampling Kantorovich Operators

In the last years the family of sampling Kantorovich operators have been widely studied for their applications to signal and digital image processing (see, e.g., [4,14–20]).

The multidimensional version of the above operators [7] are defined by

$$(K_w^{\chi} f)(\underline{x}) = \sum_{\underline{k}\in\mathbb{Z}^n} \chi(w\underline{x} - t_{\underline{k}}) \left[\frac{w^n}{A_{\underline{k}}} \int_{R_{\underline{k}}^w} f(\underline{u}) d\underline{u} \right] \quad (\underline{x} \in \mathbb{R}^n), \tag{1}$$

where $f : \mathbb{R}^n \to \mathbb{R}$ is a locally integrable function such that the above series is convergent for each $\underline{x} \in \mathbb{R}^n$, $\chi : \mathbb{R}^n \to \mathbb{R}$ represents the so called *kernel*, i.e. a function which satisfies the following assumptions (see, e.g., [6,27]):

(χ_1) $\chi \in L^1(\mathbb{R}^n)$ and it is locally bounded on the origin;
(χ_2) $\sum_{\underline{k}\in\mathbb{Z}^n} \chi(\underline{u} - t_{\underline{k}}) = 1$, for every $\underline{u} \in \mathbb{R}^n$;
(χ_3) for some $\beta > 0$, the discrete absolute moment of order β of χ is finite, i.e.,

$$m_{\beta,\Pi^n}(\chi) = \sup_{\underline{u}\in\mathbb{R}^n} \sum_{\underline{k}\in\mathbb{Z}^n} \left|\chi(\underline{u} - t_{\underline{k}})\right| \|\underline{u} - t_{\underline{k}}\|_2^{\beta} < +\infty,$$

where $\|\cdot\|_2$ is the Euclidean norm, $\Delta_{k_i} := t_{k+i} - t_k > 0$, for every $i = 1, \ldots, n$ and $\underline{k} = (k_1, \ldots, k_n) \in \mathbb{Z}^n$, where $\Pi^n := (t_{\underline{k}})_{\underline{k}\in\mathbb{Z}^n}$ a strictly monotone increasing sequence of real numbers with δ, Δ such that $\delta \le t_{k+1} - t_k \le \Delta$,

$$R_{\underline{k}}^w := \left[\frac{t_{k_1}}{w}, \frac{t_{k_1+1}}{w}\right] \times \left[\frac{t_{k_2}}{w}, \frac{t_{k_2+1}}{w}\right] \times \cdots \times \left[\frac{t_{k_n}}{w}, \frac{t_{k_n+1}}{w}\right] \quad (w > 0),$$

and $A_{\underline{k}} := \Delta_{k_1} \cdot \Delta_{k_2} \cdot \ldots \cdot \Delta_{k_n}$.

The family (1) has been firstly introduced, in its one-dimensional version, in [6] with the aim to provide an extension, to the general setting of Orlicz spaces [8,12,13], of the generalized sampling operators, introduced by P.L. Butzer in [28].

The following approximation results for the family of sampling Kantorovich operators need to be recalled in order to deal with the application to digital images and their reconstruction.

In particular, when one deals with continuous signals, the following convergence theorem holds.

Theorem 1 ([7]). *Let the kernel χ satisfy $(\chi_i), i = 1,2,3$ and let $f : \mathbb{R}^n \to \mathbb{R}$ be a continuous and bounded function. Then, for every $\underline{x} \in \mathbb{R}^n$,*

$$\lim_{w \to +\infty} (K_w^{\chi} f)(\underline{x}) = f(\underline{x}).$$

Further, if the function f is uniformly continuous and bounded, then

$$\lim_{w \to +\infty} \|K_w^{\chi} f - f\|_{\infty} = 0,$$

where $\|\cdot\|_{\infty}$ denotes the uniform norm.

Moreover, the following L^p-convergence theorem, which can be obtained as a particular case of a modular convergence theorem in Orlicz spaces, allows to reconstruct not necessarily continuous signals and hence will be useful for the application to digital images.

Theorem 2 ([7]). *Let the kernel χ satisfy $(\chi_i), i = 1,2,3$; then for every $f \in L^p(\mathbb{R}^n)$, $1 \leq p < +\infty$, we have*

$$\lim_{w \to +\infty} \|K_w^{\chi} f - f\|_p = 0,$$

and the following estimate holds

$$\|K_w^{\chi} f\|_p \leq \delta^{-n/p} (m_{0,\Pi^n}(\chi))^{(p-1)/p} \|\chi\|_1^{1/p} \|f\|_p,$$

where $\|\cdot\|_p$ denotes the usual L^p-norm.

Other than the above results, the family of sampling Kantorovich operators (1) have been extensively studied under various theoretical aspects. Indeed, the saturation order in $L^p(\mathbb{R})$-spaces and a characterization of the Favard classes for the family (1) based upon bandlimited kernels have been established in [10,11]. Furthermore, the behaviour of the first derivative of the sampling Kantorovich operators, when both differentiable and not differentiable signals are taken into account, has been studied in [9]. Finally, the family (1) has been implemented in MATLAB© and the resulting algorithm, later called SK algorithm, has been analyzed in terms of CPU time and compared with other reconstruction algorithms known in the literature in [21]. The pseudo-code of its implementation can be found in [17].

A fundamental role, in the theory of sampling Kantorovich operators, is played by the kernel function, i.e. the function which satisfies the assumptions $(\chi_1)-(\chi_3)$. In literature there are several examples of such functions, among them we can mention the one-dimensional central B-spline of order r (see, e.g., [6,27]):

$$M_r(x) := \frac{1}{(r-1)!}\sum_{i=0}^{r}(-1)^r\binom{r}{i}\left(\frac{r}{2}+x-i\right)_+^{r-1},$$

where the function $(x)_+ = \max\{x, 0\}$ denotes the positive part of $x \in \mathbb{R}$.

Its multidimensional version can be constructed from the one-dimensional one, according to the procedure provided in [29], as the following tensor product,

$$M_r^n(\underline{x}) := \prod_{i=1}^{n} M_r(x_i), \quad \underline{x} = (x_1, \ldots, x_n) \in \mathbb{R}^n.$$

Another useful class of product type kernels, which has been chosen for the reconstruction of both SCP and CC images (see Sect. 3), is given by the so called Jackson-type kernels:

$$J_k^n(\underline{x}) := \prod_{i=1}^{n} J_k(x_i), \qquad \underline{x} \in \mathbb{R}^n, \tag{2}$$

where the one-dimensional Jackson-type kernels are defined by:

$$J_k(x) = c_k sinc^{2k}\left(\frac{x}{2k\pi\alpha}\right),$$

with $x \in \mathbb{R}$, $k \in \mathbb{N}$, $\alpha \geq 1$, and where c_k is a non-zero normalization coefficient given by

$$c_k := \left[\int_{\mathbb{R}} sinc^{2k}\left(\frac{u}{2k\pi\alpha}\right) du\right]^{-1},$$

see e.g., [27]. Other than the tensor product kernels, another kind of kernels are the radial kernels. Examples of them are given by the so called Wendland kernels, which are compactly supported radial basis functions [30,31]. They are defined by considering the function

$$\phi_{m,0}(r) := (1-r)_+^m := \begin{cases} (1-r)^m, & \text{if} \quad r \leq 1 \\ 0, & \text{if} \quad r > 1 \end{cases}, \qquad r = \|\underline{x}\|_2 \qquad (\underline{x} \in \mathbb{R}^n),$$

then the Wendland kernels are defined by the following recursive formula

$$\phi_{m,k+1}(r) := \int_r^{+\infty} t\phi_{m,k}(t)dt, \quad k = 0, 1, \ldots,$$

with $r = \|\underline{x}\|_2$, $\underline{x} \in \mathbb{R}^n$ (see, e.g., [32]).

For other useful examples of kernels, see also [6,29,33,34].

Now, before applying the bidimensional sampling Kantorovich operators to image reconstruction, it is necessary to recall that a bidimensional grayscale image can be represented as:

$$I(x,y) := \sum_{i=1}^{m}\sum_{j=1}^{m} a_{ij} \cdot \mathbf{1}_{ij}(x,y) \quad (x,y) \in \mathbb{R}^2,$$

where a_{ij} are the elements of the matrix A which represents the image,

$$\mathbf{1}_{ij}(x,y) := \begin{cases} 1, & (x,y) \in (i-1,i] \times (j-1,j], \\ 0, & \text{otherwise}, \end{cases}$$

are the characteristics functions of the sets $(i-1,i] \times (j-1,j]$, $i,j = 1,2,\ldots,m$, and I is a step function, e.g. belonging to $L^p(\mathbb{R}^2)$, $1 \leq p < +\infty$, with compact support. Therefore, the family of bidimensional sampling Kantorovich operators can then be applied to the function I, considering one of the above mentioned family of kernels.

Furthermore, since it acts as a rescaling algorithm, the above implementation allows to obtain an image with an increasing information content with respect to the original one. Moreover, we remark that the SK algorithm's ability to reconstruct a given image I with any specified sampling rate is one of its key benefits: by increasing the sampling rate, it is possible to obtain an improved version of the rescaled image I.

3 Methodology

As already said, the OCTA is an innovative and clinically promising imaging technique for acquiring images of the retinal and sub-retinal vasculature. OCTA requires repeated scans at the same location to detect motion: it identifies blood vessels by detecting the blood flow-induced change in the OCT reflectance signal [1]. However, variations in flow speed and patient movements can introduce noise and artifacts into OCTA data. In order to overcome this problem, multiple en face OCTA pictures may be averaged together to attenuate noise, enhance vascular continuity, and considerably improve both qualitative and quantitative assessments [35,36]. However if we average the images without doing any other registration first, the result will be a blurred image, with a lower quality than the initial ones (see Fig. 1).

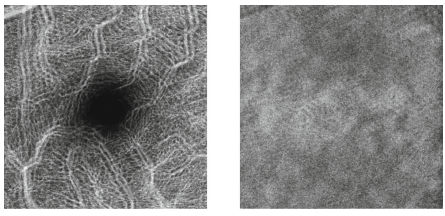


Fig. 1. Example of images averaged without a registration process: on the left an SCP (superficial capillary plexus) image; on the right a CC (choriocapillary tissue) image.

This is due to the time interval between each scan, which causes the eye to make small movements and results in image misalignment. Therefore, the first step is to register the images according to a rigid transformation (affine): the *Turboreg* plugin of *Fiji* (see, e.g., [37]), a commonly used algorithm to do motion correction, is exploited to implement the registration. It tries to align two images by minimizing their *Mean Square Error (MSE)*, while translating and rotating one of them. The Mean Square Error is a similarity index which is defined by

$$MSE = \sum_{i=1}^{M} \sum_{j=1}^{N} \frac{|I_A(i,j) - I_B(i,j)|^2}{MN},$$

where $I_A(i,j)$ and $I_B(i,j)$ are two $M \times N$ images.

However, since the eye is made up of organic tissues and fluids that are constantly deformed, a mere affine registration is not sufficient. Indeed, the resulting averaged image is still too blurred. Therefore, a supplementary type of registration is needed: a landmark based one, using the plugin *bUnwarpJ* [38], deforms elastically the image in order to align salient points previously extracted. The elastic deformations are represented by B–splines functions and the result of these operations can be seen in Fig. 2.

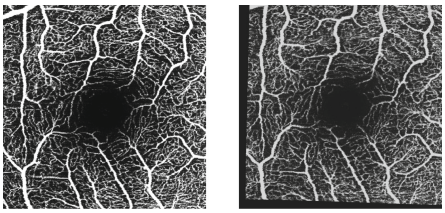


Fig. 2. Original SCP image (left) and its corresponding after both registration processes (right).

As we can see in Fig. 2, the empty space left when the registered image is dislocated, is filled with black pixels. This causes a darkening effect in the areas near the edge on the post–average image.

To detect salient points, the feature extraction plugin *Extract Mops Correspondences* has been exploited. It uses the *Difference of gaussian detector* to detect interest points according to a local feature descriptor, the *Multi-Scale Oriented Patches*, or *MOPS* [39].

At this point, every SCP image is registered on the target one, which is chosen as the less noisy. The average image obtained (Fig. 3) is now less blurred than that one in Fig. 1 and, as a result, the noise is reduced, allowing to better distinguish the vessels from the background.



Fig. 3. Example of a SCP image after the registration and averaging process.

Despite CC images pattern's makes it difficult to automatically detect fiducial points, it is possible to assume that the choriocapillary tissue is rigidly connected to the superficial capillary plexus, being them parts of the same body. For this reason, the coordinates of the transformation made on each SCP image have been saved and then applied to each corresponding CC. Therefore the final transformation on SCP and CC images is exactly the same (Fig. 4).

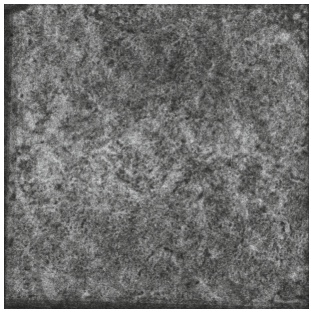


Fig. 4. Example of a CC image after the registration and averaging process.

The reconstruction process on both the SCP and CC images ends with the application of the sampling Kantorovich operator. All the images have been processed using the SK algorithm with the bidimensional Jackson type kernel (see Sect. 2) with $k = 12$ and the scaling factor $R = 2$. Note that in [4], the validity of the SK algorithm for the reconstruction of SCP images has been confirmed, in terms of the PSNR index, by the comparison with the fluorangiography reference images. Similar outcome for the CC images processed with the SK algorithm: their matching with the gold standard image, represented by a histological image, has been confirmed by a texture analysis. These results motivate the choice of the SK algorithm for the processing of the images of healthy and diabetic subjects of the present study.

The sampling Kantorovich operator offers different advantages. Indeed, it operates an integral average which acts as a *low–pass filter*, so that high frequencies are eliminated and consequently the noise is reduced. Moreover, thanks to its zooming factor, it rescales the image, increasing its information content and allowing a better analysis of the eye images, from a clinical point of view.

4 Segmentation Techniques for Cluster Counting Analysis

Starting from the assumption that the retina's vascularization ideally consists, from the anatomical point of view, of a single cluster constituted by a fully connected network [22], a segmentation procedure is needed in order to carry out a cluster counting process. For this scope, the hybrid segmentation method introduced in [4] has been exploited on SCP images, in order to overcome, from one side, the retinal vessel over–segmentation issues caused by the Phansalkar method [24], and, from the other side, the problems related to the white artifacts in the macula, caused by the local Otsu method [23], as can be seen in Fig. 5. The result of the hybrid segmentation can be seen in Fig. 6.

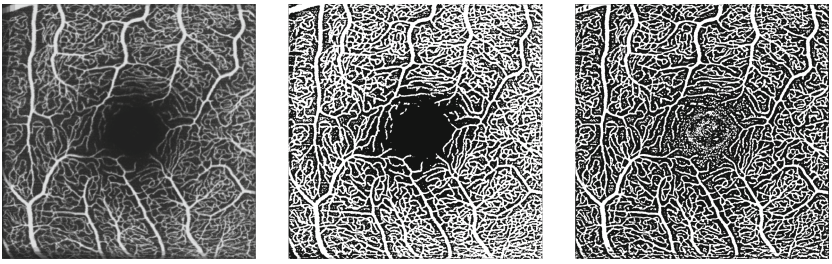


Fig. 5. An example of application of local Phansalkar thresholding (center), local Otsu thresholding (right) on the original SCP (Superficial Capillary Plexus) image (left).

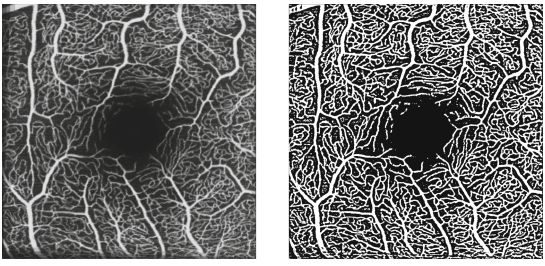


Fig. 6. Example of the application of the hybrid thresholding method (right) on a SCP image (the left).

Instead, the local Phansalkar method has been chosen for the segmentation of CC images, since it results particularly suitable when dealing with low-contrast images, characterized by a nonuniform staining (see, e.g., [25,26]), as can be seen in Fig. 7.

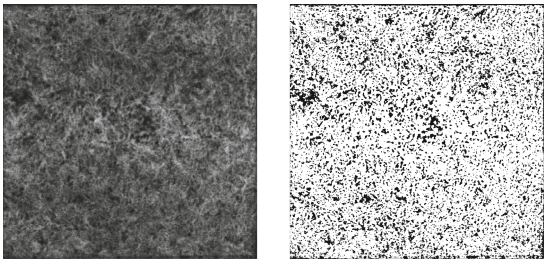


Fig. 7. Example of the application of the local Phansalkar thresholding method (right) on a CC image (left)

All these local thresholding methods have been applied with a radius of 7 pixels on the only averaged images and with a radius of 15 pixels on the images reconstructed by the SK algorithm.

5 Experimental Data

We have evaluated the above procedure on the images of thirtysix eyes from eighteen different patients. Twenty of them are clinically healthy, without any known eye disease, while the other sixteen suffer from diabetes. Even though the latter patients do not have any known eye disease, people suffering from diabetes have a high probability of developing eye pathologies, such as diabetic macular edema or diabetic retinopathy [5]. For each healthy patient eye, six SCP images and six CC images were acquired by the OCTA scan with short intervals of time between one and the other; while for diabetic subjects we have at disposal five SCP and five CC images (see Figs. 8 and 9).

The SPECTRALIS HRA+OCT2 (Heidelberg Engineering, Heidelberg, Germany) was used to capture OCTA images. This device is capable of capturing 85,000 A-scans per second with a 3.9-μm axial and 6-μm lateral resolution. It makes use of an algorithm for probabilistic amplitude decorrelation and an 870nm light source with a 50nm bandwidth. To minimize motion artifacts, TruTrack®Active Eye Tracking Technology was employed. The acquisitions were carried out using the high-resolution pre-set, with a $10° \times 10°$ (3.1 mm × 3.1 mm)-15° angle volume scan (512 B-scans with 6 m space between consecutive B-scans using an averaging technique of 5 frames/scan) centred in the foveal region. C-scan (also known as "en-face") angiograms were evaluated using the viewer software (Heyex Software, version 1.9.201.0, Heidelberg Engineering, Heidelberg, Germany). These grayscale images have been converted in 8–bit images in order to apply our processing techniques.

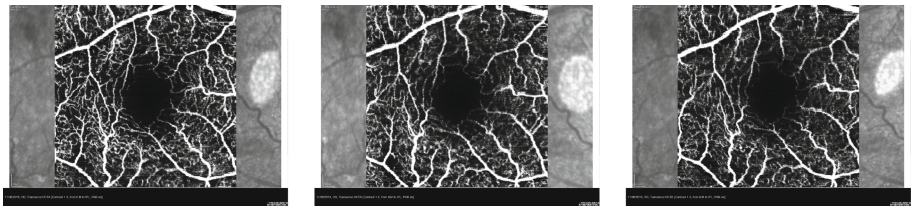


Fig. 8. Examples of three original SCP images from a diabetic patient eye.

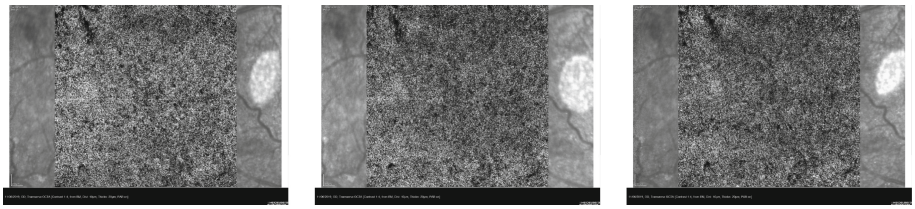


Fig. 9. Examples of three original CC images scanned at the same time of the corresponding SCP images in Fig. 8.

6 Numerical Results

In order to numerically evaluate the results obtained, we have calculated the number of connected components (clusters) of the images. The medical literature suggests that the vessels of the healthy eyes are very interconnected, and this results in a low number of clusters (ideally only one cluster). Therefore, a decrease in the cluster's number means that the results are good. Due to the above mentioned interconnection, the 8–*adjacency* criterion has been applied on the thresholded images, in order to operate a cluster counting process. In particular, we have applied the hybrid thresholding technique described in [4] on the SCP images, while the local Phansalkar method on the CC images (see, e.g., [25,26]). The cluster counting process has been done on two types of images so that comparisons can be made:

- on the averaged images where the SK algorithm has not been applied (AVG);
- on the images where the SK algorithm has been applied after the averaging process (AVG+SK).

Results are shown in the following tables.

In particular, Table 1 refers to the *SCP* images of healthy patients. The results show that the images where the SK algorithm has been applied have a lower number of clusters than the only averaged images. This represents an improvement of the image quality, as the vessels' network proves to be more connected. The same positive trend is confirmed in Table 2, showing that our image processing techniques works well also on diabetic patients' images. Indeed, the number of clusters decreases after the reconstruction, while the areas of the clusters increase.

Table 1. From the left to the right: the number describing the progressive number of healthy patients (SCP Healty Eye Nr.); the method (Method) used to process the image (AVG=averaging only, AVG+SK=SK algorithm applied after averaging); the number of clusters of the vessels' network (Nr. cluster); the mean of the area of all the previous clusters (Mean Area, in pixels) and the corresponding standard deviation (Std. Dev. Area, in pixels); the number of pixels of the whole image (Img. Pixels). The values representing areas (Mean Area and Std. Dev. Area) have been scaled according to the image dimension in order to compare the results.

SCP Healthy Eye Nr.	Method	Nr. Clusters	Mean Area	St. Dev. Area	Img. Pixels
1	AVG	1223	296.3	8819.3	902500
2	AVG	746	493.2	12571.7	902500
3	AVG	1601	234.8	7642.2	902500
4	AVG	1691	226.5	7880.0	902500
5	AVG	1536	224.7	7901.2	902500
6	AVG	1471	244.3	8763.0	902500
7	AVG	1321	289.1	9732.8	902500
8	AVG	1310	289.1	9534.8	902500
9	AVG	1526	222.0	7395.0	902500
10	AVG	1885	180.7	6634.1	902500
11	AVG	3655	69.1	1124.0	902500
12	AVG	3448	83.7	1752.3	902500
13	AVG	1315	258.3	8519.4	902500
14	AVG	1873	181.1	6485.0	902500
15	AVG	1735	214.1	6977.8	902500
16	AVG	1461	265.0	8736.2	902500
17	AVG	1508	235.7	7474.1	902500
18	AVG	1216	297.1	9124.4	902500
19	AVG	1140	326.0	10116.0	902500
20	AVG	1070	341.1	10429.0	902500
Mean		1637	248.6	7880.6	
1	AVG+SK	963	384.3	9855.9	3610000
2	AVG+SK	562	667.7	14887.6	3610000
3	AVG+SK	1241	305.6	8885.5	3610000
4	AVG+SK	1312	294.2	9032.9	3610000
5	AVG+SK	1172	298.7	9240.8	3610000
6	AVG+SK	1154	315.6	10080.8	3610000
7	AVG+SK	941	411.6	11873.5	3610000
8	AVG+SK	972	394.2	11206.4	3610000
9	AVG+SK	1226	283.3	8435.3	3610000
10	AVG+SK	1499	232.4	7543.5	3610000
11	AVG+SK	2928	94.4	1200.6	3610000
12	AVG+SK	2709	114.1	2178.3	3610000
13	AVG+SK	992	346.5	9997.7	3610000
14	AVG+SK	1281	266.3	6251.3	3610000
15	AVG+SK	1336	282.1	8152.7	3610000
16	AVG+SK	1104	356.3	10201.0	3610000
17	AVG+SK	1191	305.1	8638.4	3610000
18	AVG+SK	969	378.7	10326.5	3610000
19	AVG+SK	870	433.4	11814.9	3610000
20	AVG+SK	870	425.9	11825.6	3610000
Mean		1265	329.5	9081.5	

Table 2. From the left to the right: the number describing the progressive number of diabetic patients (SCP Diabetic Eye Nr.); the method (Method) used to process the image (AVG = averaging only, AVG+SK=SK algorithm applied after averaging); the number of clusters of the vessels' network (Nr. cluster); the mean of the area of all the previous clusters (Mean Area, in pixels) and the corresponding standard deviation (Std. Dev. Area, in pixels); the number of pixels of the whole image (Img. Pixels). The values representing areas (Mean Area and Std. Dev. Area) have been scaled according to the image dimension in order to compare the results.

SCP Diabetic Eye Nr.	**Method**	**Nr. Clusters**	**Mean Area**	**St. Dev. Area**	**Img. Pixels**
1	AVG	2748	110.4	1401.6	960400
2	AVG	1859	175.2	4100.2	960400
3	AVG	1860	181.0	2548.0	960400
4	AVG	3868	56.2	447.5	960400
5	AVG	2480	96.7	975.5	960400
6	AVG	2236	110.2	133.2	960400
7	AVG	2147	131.8	3440.7	960400
8	AVG	1795	185.6	4218.0	960400
9	AVG	2213	145.3	2138.7	960400
10	AVG	3619	89.8	871.6	960400
11	AVG	2444	131.4	1620.4	1010000
12	AVG	2559	135.8	3877.2	1010000
13	AVG	2334	96.5	2333.7	1010000
14	AVG	2402	97.3	1939.6	1010000
15	AVG	3630	67.9	609.0	1010000
16	AVG	2279	131.9	3131.4	1010000
Mean		2529	121.4	2174.1	
1	AVG+SK	2239	143.6	1455.7	3841600
2	AVG+SK	1504	222.0	3613.1	3841600
3	AVG+SK	1569	221.9	2710.8	3841600
4	AVG+SK	3473	72.3	486.8	3841600
5	AVG+SK	2035	121.5	1292.4	3841600
6	AVG+SK	1830	141.8	1442.2	3841600
7	AVG+SK	1868	159.2	2703.6	3841600
8	AVG+SK	1474	233.4	4884.0	3841600
9	AVG+SK	1780	188.7	2476.3	3841600
10	AVG+SK	3121	107.2	767.1	3841600
11	AVG+SK	2082	159.4	2762.3	4040000
12	AVG+SK	2179	162.2	4235.2	4040000
13	AVG+SK	1998	115.8	2620.4	4040000
14	AVG+SK	2022	119.34	2186.1	4040000
15	AVG+SK	3062	90.2	728.0	4040000
16	AVG+SK	1852	168.5	3576.4	4040000
Mean		2131	151.7	2371.3	

Table 3. From the left to the right: the number describing the progressive number of diabetic patients (CC Healthy Eye Nr.); the method (Method) used to process the image (AVG = averaging only, AVG+SK=SK algorithm applied after averaging); the number of clusters of the vessels' network (Nr. cluster); the mean of the area of all the previous clusters (Mean Area, in pixels) and the corresponding standard deviation (Std. Dev. Area, in pixels); the number of pixels of the whole image (Img. Pixels). The values representing areas (Mean Area and Std. Dev. Area) have been scaled according to the image dimension in order to compare the results.

CC Healthy Eye Nr.	Method	Nr. Clusters	Mean Area	St. Dev. Area	Img. Pixels
1	AVG	282	2998.1	50251.7	902500
2	AVG	278	2979.9	49412.1	902500
3	AVG	88	8963.6	84030.8	902500
4	AVG	468	1638.8	35250.4	902500
5	AVG	355	2090.0	39146.4	902500
6	AVG	305	2450.4	42103.7	902500
7	AVG	556	1418.4	33229.3	902500
8	AVG	548	1462.2	33741.6	902500
9	AVG	752	868.3	23457.0	902500
10	AVG	509	1311.6	29395.8	902500
11	AVG	2087	275.2	11832.7	902500
12	AVG	1067	638.8	20538.7	902500
13	AVG	265	2818.7	45731.4	902500
14	AVG	173	4340.9	57013.0	902500
15	AVG	1234	498.8	16991.8	902500
16	AVG	441	1693.6	35407.8	902500
17	AVG	473	1447.3	31289.3	902500
18	AVG	565	1157.2	27330.4	902500
19	AVG	453	1653.6	34929.9	902500
20	AVG	492	1474.7	32459.3	902500
Mean		570	2109.0	36677.2	
1	AVG+SK	214	4044.7	59051.4	3610000
2	AVG+SK	206	4107.6	58658.3	3610000
3	AVG+SK	38	21475.8	132354.2	3610000
4	AVG+SK	363	2171.9	41158.6	3610000
5	AVG+SK	199	9310.1	54955.0	3610000
6	AVG+SK	201	3921.3	54699.7	3610000
7	AVG+SK	429	1911.3	39353.9	3610000
8	AVG+SK	318	2622.3	46446.9	3610000
9	AVG+SK	510	1375.3	30856.4	3610000
10	AVG+SK	263	2747.8	44436.0	3610000
11	AVG+SK	1462	425.3	15581.6	3610000
12	AVG+SK	704	1033.9	27181.3	3610000
13	AVG+SK	111	7080.2	74523.0	3610000
14	AVG+SK	129	5957.4	67586.0	3610000
15	AVG+SK	563	1230.3	28927.9	3610000
16	AVG+SK	282	2794.7	46819.6	3610000
17	AVG+SK	236	3146.8	48211.2	3610000
18	AVG+SK	301	2383.3	41241.6	3610000
19	AVG+SK	353	2183.2	40767.3	3610000
20	AVG+SK	408	1854.0	37155.0	3610000
Mean		365	3788.9	49496.7	

Table 4. From the left to the right: the number describing the progressive number of diabetic patients (CC Diabetic Eye Nr.); the method (Method) used to process the image (AVG = averaging only, AVG+SK=SK algorithm applied after averaging); the number of clusters of the vessels' network (Nr. cluster); the mean of the area of all the previous clusters (Mean Area, in pixels) and the corresponding standard deviation (Std. Dev. Area, in pixels); the number of pixels of the whole image (Img. Pixels). The values representing areas (Mean Area and Std. Dev. Area) have been scaled according to the image dimension in order to compare the results.

CC Diabetic Eye Nr.	**Method**	**Nr. Clusters**	**Mean Area**	**St. Dev. Area**	**Img. Pixels**
1	AVG	2782	209.8	10154.7	960400
2	AVG	4928	77.5	1213.6	960400
3	AVG	1414	450.0	16129.1	960400
4	AVG	2685	207.3	9860.5	960400
5	AVG	4098	107.8	4754.2	960400
6	AVG	3242	140.1	5216.3	960400
7	AVG	794	943.6	26180.5	960400
8	AVG	410	1891.4	38066.7	960400
9	AVG	1925	306.4	12690.1	960400
10	AVG	3734	122.1	4472.3	960400
11	AVG	159	5555.9	69979.1	1010000
12	AVG	843	842.9	23518.3	1010000
13	AVG	1224	584.9	19892.0	1010000
14	AVG	938	766.2	23139.4	1010000
15	AVG	3864	131.8	5528.1	1010000
16	AVG	4664	86.3	1136.1	1010000
Mean		2357	776.5	16995.7	
1	AVG+SK	1967	322.1	13398.3	3841600
2	AVG+SK	3910	104.0	2461.4	3841600
3	AVG+SK	749	956.9	25729.2	3841600
4	AVG+SK	1780	351.2	14057.1	3841600
5	AVG+SK	3106	155.5	6371.8	3841600
6	AVG+SK	2298	220.0	8929.5	3841600
7	AVG+SK	580	1364.9	32578.7	3841600
8	AVG+SK	217	3830.1	56265.5	3841600
9	AVG+SK	1047	638.2	20070.6	3841600
10	AVG+SK	2603	197.6	7808.6	3841600
11	AVG+SK	96	9568.7	93701.4	4040000
12	AVG+SK	567	1323.4	30844.0	4040000
13	AVG+SK	767	1010.3	27368.8	4040000
14	AVG+SK	568	1386.5	32845.2	4040000
15	AVG+SK	2508	232.9	10592.7	4040000
16	AVG+SK	3441	130.0	3094.4	4040000
Mean		1638	1362.0	24132.3	

The results shown in Tables 3 and 4 indicate that the process works well for CC images, too. When the SK algorithm is applied, increases the links between vessels also in case of CC images.

The above cluster counting analysis shows a stronger vessel's connection, both for SCP and CC images, whenever the SK algorithm is applied. Moreover, we point out that the variation in size of the images taken into account does not affect the analysis performed. Indeed, the comparisons have been made between one AVG image and its corresponding AVG+SK image, having the foresight to scale the values representing areas. Instead, for what concerns the number of clusters, it has been tested that a larger sized image results in a greater number of clusters. Indeed, by duplicating (without interpolation) the size of the only averaged images, the number of clusters increases. As a consequence, the results achieved on the images reconstructed by the SK algorithm are not only the most reliable, since the number of clusters decreases, but also the most conservatives, since we obtain a lower number of connected regions on a double sized image with respect to the only averaged one.

Finally, we note that diabetic patients' images have a number of clusters on average higher than healthy patients, confirming the clinical incidence of the disease on retinal pathologies.

7 Conclusions

For the processing and improvement of digital images, the reconstruction capabilities of sampling Kantorovich operators have proved to be highly beneficial. Indeed, in [4] it has been already shown that the SK algorithm improves both the quality of SCP and CC images of healthy subjects. In the present study, we extend the analysis also on diabetic subjects: after registration and averaging processes, the SK algorithm is applied in order to rescale and enhance the eye images of the healthy and diabetic patients considered. By exploiting the hybrid thresholding technique presented in [4], the SCP images are binarized, avoiding the retinal vessel over-segmentation and the white artifacts in the macula, caused respectively by local Phansalkar's and Otsu's thresholding methods. A novel approach of this study consists in the application of the local Phansalkar thresholding technique on the CC images, as it results particularly suitable on low-contrast images, characterized by nonuniform staining (see, e.g., [25,26]).

Finally, a cluster counting analysis has been conducted by finding the connected regions in the thresholded images, according to the 8–adjacency criterion. This choice is motivated by the fact that retina vessels' network is assumed to be ideally fully connected. The cluster counting process proved that the images reconstructed by the SK algorithm (after the averaging process) have a lower number of clusters than the only averaged images. Indeed, it improves the representation of vessels' network, as it acts as a resizing algorithm and as a low-pass filter, eliminating the noise contained in high frequencies, also on diabetic patients, who are prone to eye diseases. The variation of the number of clusters between healthy and diabetic patients can be used to analyze the differences

between the retinal trees of the two categories, which results to be a clinical indication of the disease.

In conclusion, the outcome of our study shows an effective improvement on the image quality, and, consequently, a more accurate medical diagnosis of eye diseases that can be observed both from a visual and a numerical point of view.

Acknowledgements. The authors wish to thank prof. C. Cagini and prof. M. Lupidi of the Ophthalmology Section of the Department of Medicine and Surgery of the University of Perugia for having kindly provided the images used in this work.

Moreover, A. Travaglini and G. Vinti are members of the Gruppo Nazionale per l'Analisi Matematica, la Probabilitá e le loro Applicazioni (GNAMPA) of the Istituto Nazionale di Alta Matematica (INdAM), of the network RITA (Research ITalian network on Approximation) and of the UMI group "Teoria dell'Approssimazione e Applicazioni."

References

1. Hagag, A.M., Gao, S.S., Jia, Y., Huang, D.: Optical coherence tomography angiography: technical principles and clinical applications in ophthalmology. Taiwan J. Ophthalmol. **7**(3), 115–129 (2017)
2. Sakamoto, A., Hangai, M., Yoshimura, N.: Spectral-domain optical coherence tomography with multiple B-scan averaging for enhanced imaging of retinal diseases. Ophthalmology **115**(6), 1071–1078 e7 (2008)
3. Sander, B., Larsen, M., Thrane, L., Hougaard, J.L., Jorgensen, T.M.: Enhanced optical coherence tomography imaging by multiple scan averaging. Br. J. Ophthalmol. **89**(2), 207–212 (2005)
4. Cagini, C., et al.: Improvement of retinal OCT angiograms by Sampling Kantorovich algorithm in the assessment of retinal and choroidal perfusion. Appl. Math. Comput. **427**(4), 127152 (2022)
5. Skarbez, K., Priestley, Y., Hoepf, M., Koevary, S.B.: Comprehensive review of the effects of diabetes on ocular health. Expert Rev. Ophthalmol. **5**(4), 557–577 (2010)
6. Bardaro, C., Butzer, P.L., Stens, R.L., Vinti, G.: Kantorovich-type generalized sampling series in the setting of Orlicz spaces. Sampling Theory Signal Image Process. **6**(1), 29–52 (2007)
7. Costarelli, D., Vinti, G.: Approximation by multivariate generalized sampling Kantorovich operators in the setting of Orlicz spaces. Bollettino dell'Unione Matematica Italiana **4**(3), 445–468 (2011)
8. Bardaro, C., Musielak, J., Vinti, G.: Nonlinear Integral Operators and Applications. De Gruyter Series in Nonlinear Analysis and Applications, New York, Berlin (2003)
9. Cantarini, M., Costarelli, D., Vinti, G.: Approximation of differentiable and not differentiable signals by the first derivative of sampling Kantorovich operators. J. Math. Anal. Appl. **509**(1), Art. Number 125913 (2021)
10. Costarelli, D., Vinti, G.: Saturation by the Fourier transform method for the sampling Kantorovich series based on bandlimited Kernels. Anal. Math. Phys. **9**(4), 2263–2280 (2019). https://doi.org/10.1007/s13324-019-00334-6
11. Costarelli, D., Vinti, G.: Approximation properties of the sampling Kantorovich operators: regularization, saturation, inverse results and Favard classes in L^p-spaces. J. Fourier Anal. Appl. **28**, 1–42 (2022)

12. Musielak, J.: Orlicz Spaces and Modular Spaces, 1st edn. LNM. Springer, Berlin (1983). https://doi.org/10.1007/BFb0072210
13. Rao, M.M., Ren, Z.D.: Theory of Orlicz Spaces. Dekker Inc., New York-Basel-Hong Kong (1991)
14. Asdrubali, F., et al.: Mathematical models for the improvement of detection techniques of industrial noise sources from acoustic images. Math. Methods Appl. Sci. **44**(13), 10448–10459 (2021)
15. Cluni, F., Gusella, V., Vinti, G.: Masonry elastic characteristics assessment by thermographic images. Meccanica **54**(9), 1339–1349 (2019)
16. Costarelli, D., Pozzilli, P., Seracini, M., Vinti, G.: Enhancement of cone-beam computed tomography dental-maxillofacial images by sampling Kantorovich algorithm. Symmetry **13**(8), Art. number 1450 (2021)
17. Costarelli, D., Seracini, M., Travaglini, A., Vinti, G.: Alzheimer biomarkers esteem by sampling Kantorovich algorithm. Math. Methods Appl. Sci. 1–15 (2023). https://doi.org/10.1002/mma.9268
18. Costarelli, D., Seracini, M., Vinti, G.: A segmentation procedure of the pervious area of the aorta artery from CT images without contrast medium. Math. Methods Appl. Sci. **43**(1), 114–133 (2020)
19. Osowska-Kurczab, A., et al.: Improvement of renal image recognition through resolution enhancement. Expert Syst. Appl. **213**(4), 118836 (2023)
20. Travaglini, A., Vinti, G., Scalera, G.B., Scialpi, M.: A large scale analysis for testing a mathematical model for the study of vascular pathologies. Mathematics **11**(8), Art. Number 1831 (2023)
21. Costarelli, D., Seracini, M., Vinti, G.: A comparison between the sampling Kantorovich algorithm for digital image processing with some interpolation and quasi-interpolation methods. Appl. Math. Comput. **374**(2) (2020)
22. Provis, J.M.: Development of the primate retinal vasculature. Prog. Retin. Eye Res. **20**(6), 799–821 (2001)
23. Otsu, N.: A threshold selection method from Gray-level histograms. IEEE Trans. Syst. Man Cybern. Syst. **9**(1), 62–66 (1979)
24. Phansalkar, N., More, S., Sabale, A., Joshi, M.: Adaptive local thresholding for detection of nuclei in diversity stained cytology images. In: International Conference on Communications and Signal Processing, pp. 218–220 (2011)
25. Laiginhas, R., Cabral, D., Falcão, M.: Evaluation of the different thresholding strategies for quantifying choriocapillaris using optical coherence tomography angiography. Quant. Imaging Med. Surg. **10**(10), 1994–2005 (2020)
26. Spaide, R.F.: Choriocapillaris flow features follow a power law distribution: implications for characterization and mechanisms of disease progression. Am. J. Ophthalmol. **170**, 58–67 (2016)
27. Butzer, P.L., Nessel, R.J.: Fourier Analysis and Approximation, 1st edn. Academic Press, New York-London (1971)
28. Butzer, P.L.: A survey of the Whittaker-Shannon sampling theorem and some of its extensions. J. Math. Res. Exposition **3**, 185–212 (1983)
29. Butzer, P.L., Fischer, A., Stens, R.L.: Generalized sampling approximation of multivariate signals; theory and some applications. Note di Matematica **10**(1), 173–191 (1990)
30. Wendland, H.: Piecewise polynomial, positive definite and compactly supported radial functions of minimal degree. Adv. Comput. Math. **4**, 389–396 (1995)
31. Wendland, H.: Scattered Data Approximation, Cambridge Monographs on Applied and Computational Mathematics, vol. 17. Cambridge University Press, Cambridge (2005)

32. Costarelli, D., Piconi, M., Vinti, G.: The multivariate Durrmeyer-sampling type operators in functional spaces. Dolomites Res. Notes Approx. **15**, 128–144 (2023)
33. Kivinukk, A., Tamberg, G.: On approximation properties of sampling operators by dilated Kernels. In: 8th International Conference on Sampling Theory and Applications, SampTA 2009, Marseille, 18–22 May 2009
34. Orlova, O., Tamberg, G.: On approximation properties of generalized Kantorovich-type sampling operators. J. Approx. Theory **201**, 73–86 (2016)
35. Uji, A., Balasubramanian, S., Lei, J., Baghdasaryan, E., Al-Sheikh, M., Sadda, S.R.: Impact of multiple En Face image averaging on quantitative assessment from optical coherence tomography angiography images. Ophthalmology **124**(7), 944–952 (2017)
36. Uji, A., et al.: Multiple enface image averaging for enhanced optical coherence tomography angiography imaging. Acta Ophthalmol. **96**(7), 820–827 (2018)
37. Thévenaz, P., Ruttimann, U.E., Unser, M.A.: A pyramid approach to subpixel registration based on intensity. IEEE Trans. Image Process. **7**(1), 27–41 (1998). A Publication of the IEEE Signal Processing Society
38. Arganda-Carreras, I., Sorzano, C.O., Kybic, J., Ortíz-de-Solórzano, C.: bUnwarpJ : consistent and elastic registration in ImageJ. In: Methods and Applications (2008)
39. Brown, M., Szeliski, R., Winder, S.: Multi-image matching using multi-scale oriented patches. In: Proceedings of the 2005 IEEE Computer Society Conference on Computer Vision and Pattern Recognition, vol. 1, pp. 510–517 (2005)